Suppression and enhancement of vibrational resonance by time-periodic phase-modulation in a driven gyroscope

P. O. Adesina*
Department of Physical Sciences, Redeemer's University, Ede 232101, Nigeria and Department of Physics, University of Ibadan, Ibadan 200284, Nigeria

U. E. Vincent†
Department of Physical Sciences, Redeemer's University, Ede 232101, Nigeria and Department of Physics, Lancaster University, Lancaster LA1 4YB, United Kingdom

T. O. Roy-Layinde
Department of Physics, Olabisi Onabanjo University, Ago-Iwoye 120107, Nigeria

O. T. Kolebaje
Department of Physics, Adeyemi Federal University of Education, Ondo 350106, Nigeria

O. O. Popoola
Department of Physics, University of Ibadan, Ibadan 200284, Nigeria

P. V. E. McClintock
Department of Physics, Lancaster University, Lancaster LA1 4YB, United Kingdom
(Dated: April 15, 2025)

We have investigated the dynamics of a phase-modulated driven gyroscope, including vibrational resonance (VR) phenomena and the stability of the system, both with and without the phase modulation. For appropriate choices of parameters, three distinct equilibrium states can be attained. We use the method of direct separation of the fast and slow motions to show that, in the presence of an additive external driving force, time-periodic phase-modulation promotes resonance suppression. Both giant VR and anti-resonance induction in the quiescent state arise within certain parameter ranges. The implications of the giant and suppressed resonances for gyroscope applications and beyond are discussed.

Keywords: Gyroscope, Phase-modulation, Dual-frequency forces, Vibrational resonance

I. INTRODUCTION

For over a century, the gyroscope has played a significant role in advancing modern technology. It has attracted research interest in physics and engineering, especially in aerodynamics. Gyroscopes are spinning devices that are fixed to a frame, with the ability to detect an angular velocity as the frame rotates [1]. They are widely used in navigation systems [2], aerospace engineering [1], robotics [3], and in many other fields where stability and precise measurement of angular motion are essential. The main feature of a gyroscope device is to maintain the axis of a spinning rotor. Gyroscopes are unique in their characteristic effects [4], for which there is a well-developed mathematical formulation based on the conservation of kinetic energy and angular momentum [5]. Depending on the underlying physical principles and the technology involved, there are several different types of gyroscope, including: conventional mechanical gyroscopes; optical gyroscopes, which include both fiber optic gyroscopes (FOGs) and ring laser gyroscopes (RLGs) [1]; MEMs (micro-electro-mechanical systems) gyroscopes; and MOEMs (micro-opto-electro-mechanical systems) gyroscopes [6]. Understanding the dynamics of a gyroscope requires an examination of its rotational motion, its equilibrium conditions, and its response to external forces. It is this latter question that provides the main focus of the present paper.

A system's response to external forces has been one of the key research foci of nonlinear dynamics. When there are two external periodic forces of sufficiently different frequency the response, whether enhancement or suppression, is known as vibrational resonance (VR) [7–10]. VR is closely related to stochastic resonance (SR) where a weak periodic force in a nonlinear system can be enhanced/suppressed by the input zero-mean noise [11, 12], the main difference being that, in VR, the role of noise is replaced by that of a high-frequency (HF) force.

Studies of both SR and VR have grown tremendously in recent years, and potential applications abound. These include bulk material processing [9], signal processing [13, 14], optical communication systems [15, 16], image processing [17, 18], logic gate operations [19, 20], energy harvesting [21, 22], bearing defect detection in machin-

* po.adesina@ui.edu.ng
† Corresponding author:u.vincent@lancaster.ac.uk

ery [23–25], molecular vibrations [26, 27] and inertial navigational aid in gyroscope systems [28, 29]. Comprehensive reviews have been presented on different varieties of VR and their applications [9, 10, 30].

Following the original observation of VR [7], several interesting works have been completed on this topic, and on related multi-frequency induced dynamics, thereby enriching our knowledge of a broad range of multi-frequency driven nonlinear systems [9, 10, 28, 30–37]. Among these studies, modulation of the system parameters, including the amplitude and frequency of the external driving force, has been receiving attention because they constitute the building blocks of communication systems, as well as signal amplification, sensing and filtering [38–40]. In this direction, Oyeleke *et al.* [28] recently reported VR in a parametrically-excited gyroscope, where the amplitude of the potential function was modulated by a time-periodic force. More recently, Nashrin *et al.* [41] analysed VR in a variety of double-well quintic oscillators by modulating the natural frequency of the oscillator. In another development, Adéyémi *et al.* [37] investigated the impact of cooperation between time-periodic parametric dissipation and an amplitude-modulated signal on the occurrence of torus-doubling bifurcations, and on VR in an asymmetric mixed Rayleigh-Liénard driven oscillator. Similarly, Kolebaje *et al.* [42] studied VR in a charged bubble oscillator driven by a modulated acoustic field, where it was shown that VR occurred at relatively low values of the acoustic driving pressure.

For nonlinear systems characterized by phase variables, such as the Kuramoto-Sakaguchi and Stuart-Landau oscillators [43], molecular rotors and enzymatic substrates [44], superconducting Josephson junctions [45–48], phase-locked loops [49], spin-torque oscillators [50] and gyroscope models [28, 51, 52], to mention only a few examples, time-periodic phase modulation offers a promising approach for controlling the dynamics and response of the system. For instance, so-called absolute negative mobility (ANM) was achieved and reported by Dandogbessi and Kenfack [53] in a periodic potential substrate with time-periodic phase modulation. In another development, it was shown that time-periodic modulation of the potential produced a remarkable impact on the transmission probability and conductance of an MoS_2-based circuit [54, 55]. Systems with periodic phase modulation have important applications in communication, optical tweezers, neurology, and astronomy [56, 57]. Some earlier experimental works have demonstrated the spectral efficacy of time-periodic phase modulation in the control of short laser pulses in plasma channels [58, 59], vibrational modes of trapped ions [60], ultrafast transmission of electrons [61] and ultrashort light pulses [62].

Very recently [48], we reported distinct phase modulation effects in a Josephson junction model with high-frequency time-periodic phase modulation [48], namely, resonant induction and resonant amplification, leading to the appearance of a double resonance for the driven oscillator. Here, we explore use of the time-periodic phase

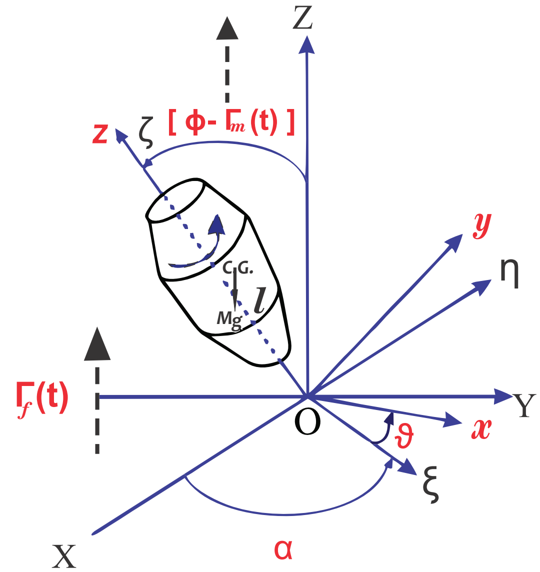

FIG. 1. [Color online] Schematic diagram of a phase-modulated gyroscope. For definitions of the variables, see text.

modulation technique to investigate VR in a gyroscope model driven by a time-periodic force. We provide both theoretical and numerical evidence that multiple, significantly enhanced and weakly attenuated resonances can be achieved within appropriate phase parameter regimes when the gyroscope's phase is modulated. The ability of gyroscopes to detect small angular velocity changes makes them especially valuable for applications where high precision is required, such as those that arise in aerospace and defense. Thus, our novel VR approach has the potential to chart a new course for the application of time-periodic phase-modulation in navigation, robotics, and space exploration.

The paper is organized as follows: The model and its stability are presented in Section II. The main results are developed and discussed in Section III, while Sec. IV concludes the paper.

II. MODEL AND STABILITY ANALYSIS

The equation of motion governing the gyroscope depicted schematically in Fig. 1 was derived in Refs.[28, 51]. It can be written in dimensionless form as:

$$\ddot{\phi} + b_1\dot{\phi} + b_2\dot{\phi}^3 + \frac{dV(\phi,t)}{d\phi} = \Gamma_f(t), \tag{1}$$

where the nutation ϕ, precession α, and spin ϑ, are related to Euler angles. The phase-modulated gyroscope potential $V(\phi, t)$, in the absence of the external driving force, can be written as:

$$V(\phi,t) = \frac{\beta^2}{(1+\cos\phi)} + A\cos(\phi - \Gamma_m(t)). \tag{2}$$

The time-periodic phase modulating function, $\Gamma_m(t) = g\sin(\Omega t)$ is considered as the high-frequency (HF) force in this case, while $\Gamma_f(t) = f\sin(\omega t)$ is the external low-frequency (LF) force. The parameters g and f represent the amplitudes of the HF and LF periodic forces, respectively; $b_1\dot{\phi} + b_2\dot{\phi}^3$ represents the linear and cubic nonlinear damping terms. The conventional VR scenario requires that $\Omega \gg \omega$.

To analyze the stability of the system, Eq. (1) can be reformulated into a system of coupled first-order differential equations:

$$\begin{aligned} \dot{\phi} &= y, \\ \dot{y} &= -b_1 y - b_2 y^3 - \frac{\beta^2(1-\cos\phi)^2}{\sin^3\phi} + A\sin(\phi), \end{aligned} \tag{3}$$

where we have assumed that applied forces are absent. The equilibrium points $(\phi^*, 0)$ of equation (3) were determined by solving:

$$\sin(\phi^*)\left(\frac{\beta^2}{(1+\cos\phi^*)^2} - A\right) = 0. \tag{4}$$

There are five (5) such possible equilibria $(\phi^*, 0)$, given by

(i) $\phi_1^* = n\pi,$ for $n \in \mathbb{Z}$,

(ii) $\phi_{2,3}^* = \pm\arccos\left(\frac{\beta}{\sqrt{A}} - 1\right) + 2n\pi,$ for $n \in \mathbb{Z}$, and

(iii) $\phi_{4,5}^* = \pm\arccos\left(-\frac{\beta}{\sqrt{A}} - 1\right) + 2n\pi,$ for $n \in \mathbb{Z}$.

By imposing the geometrical restriction $-\pi \le \phi \le \pi$, the feasible equilibria reduce to

$$\phi_1^* = 0, \qquad \phi_{2,3}^* = \pm\arccos\left(\frac{\beta}{\sqrt{A}} - 1\right).$$

The Jacobian matrix J evaluated at these equilibria $(\phi^*, 0)$ is

$$J = \begin{pmatrix} 0 & 1 \\ P & -b_1 \end{pmatrix}. \tag{5}$$

where

$$P = A\cos\phi^* - \frac{2\beta^2}{1+\cos\phi^*} + \frac{3\beta^2\cos\phi^*}{(1+\cos\phi^*)^2}.$$

The characteristic equation of J is $\lambda^2 + b_1\lambda - P = 0$. According to the Routh-Hurwitz stability criterion, the equilibrium $(\phi^*, 0)$ is stable if $b_1 > 0$ and $P < 0$. For the equilibrium point $(0,0)$, $P = A - \beta^2/4$. Hence, $(0,0)$ is stable for $\beta > 2\sqrt{A}$ and unstable otherwise, provided b_1 is kept positive. The equilibria $(\phi_{2,3}^*, 0)$ are stable when $\beta < 2\sqrt{A}$ and unstable otherwise. Thus, the critical point $\beta = 2\sqrt{A}$ marks a pitchfork bifurcation, where two new equilibria, $(\phi_{2,3}^*, 0)$, emerge from the single equilibrium $(0,0)$ as shown in Figure 2. Consequently, in

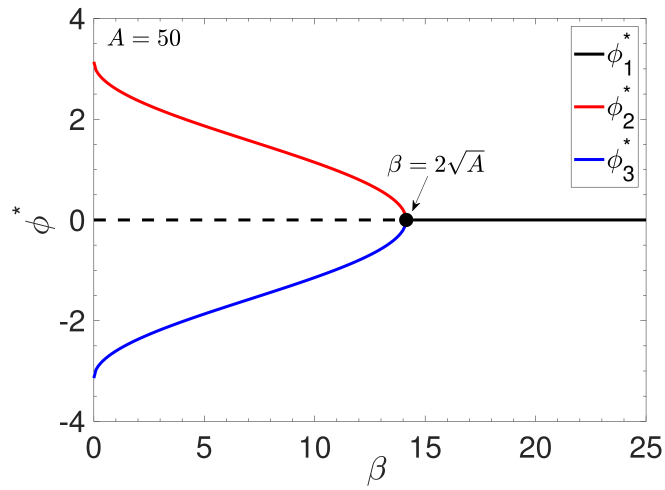

FIG. 2. [Color online] Bifurcation diagram of fixed points against β for $A = 200$. A pitchfork bifurcation is observed, as illustrated. The equilibrium point $\phi = 0$ (black line) is stable for $\beta > 2\sqrt{A}$ (solid black line) and unstable for $\beta < 2\sqrt{A}$ (dashed black line). For $\beta < 2\sqrt{A}$, two additional stable equilibria, $\phi_2^* = \arccos\left(\beta/\sqrt{A} - 1\right)$ (red line) and $\phi_3^* = -\arccos\left(\beta/\sqrt{A} - 1\right)$ (blue line), emerge. The bold black dot indicates the bifurcation point at $\beta = 2\sqrt{A}$.

the absence of the phase modulating force, the potential $V(\phi, t)$ exhibits either a single or a double-well configuration, depending on the values of A and β. Specifically, for $\beta < 2\sqrt{A}$, the potential forms a double-well with symmetric minima at ϕ_2 and ϕ_3. For $\beta > 2\sqrt{A}$, it forms a single-well with a minimum at $\phi = 0$. Figure 3 shows the the parameter space for which double-well and single-well structures can appear. For instance, a single-well structure was obtained when $A = 1$, $\beta = 10$, $\Omega = 50$ and $t = 1$ as depicted in Fig. 4(a), while a double-well structure is shown in Fig. 4(b) when $A = 500$, $\beta = 4$, $\Omega = 50$ and $t = 1$. The potential structure can be switched between single-well and double-well by tuning the parameters β and A. The single-well's equilibrium point is located in the region where oscillations occur along the gyroscope's major axis, around $\phi = -1$.

Upon introducing a time-periodic phase modulation force to the potential $V(\phi, t)$, the trivial equilibrium $\phi_1^* = 0$ is no longer valid. The new equilibria are determined by the real roots of

$$(x+1)^2\cos G - \frac{x(x+1)^2}{\sqrt{1-x^2}}\sin G - \frac{\beta^2}{A} = 0,$$

where $x = \cos\phi$ and $G = g\sin(\Omega t)$. Under this scenario, the potential $V(\phi, t)$ retains its single-well or double-well nature but can become asymmetric depending on the values of A and β as well as on the parameters of the modulation. The impacts of the amplitude (g) of the phase modulation on both the double-well and single-well structures are shown in Fig. 4 for $g = 0, 1, 2$ and 5. Evidently,

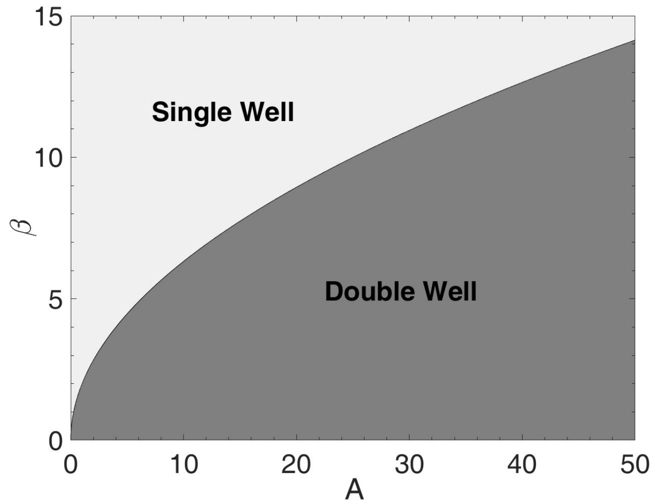

FIG. 3. Two-parameter bifurcation diagram indicating regions of double-well potential (dark grey) and single-well potential (light gray).

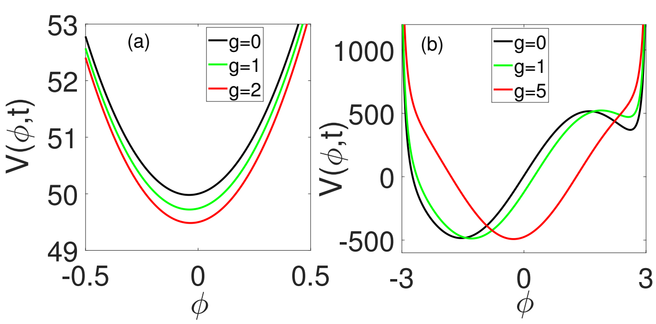

FIG. 4. [Color online] The potential of the system (1) versus ϕ. (a) Single-well system ($\beta = 10$, $A = 1$, $\Omega = 50$, $t = 1$), showing the impact of phase modulation from $g = 0$ (zero-phase) to $g = 1$ and $g = 2$. (b) Double-well system ($\beta = 4$, $A = 500$, $\Omega = 50$, $t = 1$), showing the impact of phase modulation from $g = 0$ (zero-phase) to $g = 1$ and $g = 5$.

the potential structure can be switched from double-well to single-well by tuning the amplitude, g. Moreover, the depth of the potential well decreases with increase in g. Notably, the asymmetric double-well potential exhibits a local maximum and minima for $g = 0$ at $\phi = 1.5$ and $\phi = -1.7$ (a more stable equilibrium point), and $\phi = 2.7$ respectively. As the g value increases from 0 to 5, one of the two local minima in the double-well potential located at $\phi = -1.7$ is continuously shifted rightward with a corresponding reduction in the depth of the other local minimum, which is located at $\phi \approx 2.7$.

III. ANALYSIS OF VIBRATIONAL RESONANCE (VR)

A. Case 1: $\Gamma_m(t) = g\sin(\Omega t)$, $\Gamma_f(t) = f\sin(\omega t)$

First, we analyse the motion of the gyroscope by separating the variables into those describing rapid and slow motions, respectively. This results in two differential equations. Based on the condition that $\Omega \gg \omega$, we seek the solution of the nutation angle $\phi(t)$ of the gyroscope system (1), assuming it to be the superposition of two solutions, namely: $\epsilon(t)$ of the slow motion propagation with frequency ω, period $2\pi/\omega$; and $\mu(t, \Omega t)$, period 2π of the fast oscillations with frequency Ω, in the fast time $\tau = \Omega t$. Thus

$$\phi(t) = \epsilon(t) + \mu(t, \Omega t). \tag{6}$$

To facilitate this analysis, the function $\sin[\phi - g\sin(\Omega t)]$ can be re-expressed as:

$$\begin{aligned} \sin[\phi - g\sin(\Omega t)] = {} & \sin(\phi)\cos(g\sin(\Omega t)) \\ & - \sin(g\sin(\Omega t))\cos(\phi). \end{aligned} \tag{7}$$

This reduces Eq. (1) to:

$$\begin{aligned} & \ddot{\epsilon} + \ddot{\mu} + b_1\dot{\epsilon} + b_1\dot{\mu} + b_2(\dot{\epsilon} + \dot{\mu})^3 \\ & + \frac{\beta^2[1 - \cos(\epsilon)\cos(\mu) + \sin(\epsilon)\sin(\mu)]^2}{[\sin(\epsilon)\cos(\mu) + \sin(\mu)\cos(\epsilon)]^3} \\ & - A[(\sin(\epsilon)\cos(\mu) + \sin(\mu)\cos(\epsilon))\cos(g\sin(\Omega t)) \\ & - (\cos(\epsilon)\cos(\mu) - \sin(\epsilon)\sin(\mu))\sin(g\sin(\Omega t))] \\ & = f\sin(\omega t). \end{aligned} \tag{8}$$

The mean values for the fast oscillation are given as:

$$\begin{aligned} \langle \mu \rangle &= \frac{1}{2\pi}\int_0^{2\pi} \mu d\tau = 0, \\ \langle \cos(g\sin(\Omega t)) \rangle &= J_0(g), \\ \langle \sin(g\sin(\Omega t)) \rangle &= 0, \\ \langle \sin\mu \rangle &= \frac{1}{2\pi}\int_0^{2\pi} \sin\mu d\tau = 0, \\ \langle \cos\mu \rangle &= \frac{1}{2\pi}\int_0^{2\pi} \cos\mu d\tau = J_0(\mu_0), \end{aligned} \tag{9}$$

where $J_0(\mu_0)$ and $J_0(g)$ represent zeroth order Bessel functions of the first kind. We apply the expression in Eq. (9) to average both sides of Eq. (8) over the period 2π and interval $[0, \frac{2\pi}{\Omega}]$, so that:

$$
\begin{aligned}
&\ddot{\epsilon} + b_1\dot{\epsilon} + b_2\dot{\epsilon}^3 \\
&\quad + \frac{\beta^2[1-\cos(\epsilon)\langle\cos(\mu)\rangle + \sin(\epsilon)\langle\sin(\mu)\rangle]^2}{[\sin(\epsilon)\langle\cos(\mu)\rangle + \langle\sin(\mu)\rangle\cos(\epsilon)]^3} \\
&\quad - A[(\sin(\epsilon)\langle\cos(\mu)\rangle \\
&\quad + \langle\sin(\mu)\rangle\cos(\epsilon))\langle\cos(g\sin(\Omega t))\rangle \\
&\quad - (\cos(\epsilon)\langle\cos(\mu)\rangle - \sin(\epsilon)\langle\sin(\mu)\rangle)\langle\sin(g\sin(\Omega t))\rangle] \\
&\quad = f\sin(\omega t).
\end{aligned} \tag{10}
$$

In order to obtain the equation of fast motion, we subtract Eq. (10) from Eq. (8) and, by using the inertial approximation i.e. $\ddot{\mu} \gg \dot{\mu} \gg \mu$, we then have:

$$
\begin{aligned}
&\ddot{\mu} + b_1\dot{\mu} + b_2\dot{\mu}^3 + 3b_2\dot{\mu})^2\dot{\epsilon} + 3b_2\dot{\epsilon})^2\dot{\mu}) \\
&+ \frac{\beta^2[1-\cos(\epsilon)(r_1) + \sin(\epsilon)(r_2)]^2}{[\sin(\epsilon)(r_3) + \cos(\epsilon)(r_4)]^3} \\
&- A[(\sin(\epsilon)\cos(\mu) + \sin(\mu)\cos(\epsilon))\cos(g\sin(\Omega t)) \\
&- (\sin(\epsilon)\langle\cos(\mu)\rangle + \langle\sin(\mu)\rangle\cos(\epsilon))\langle\cos(g\sin(\Omega t))\rangle \\
&- (\cos(\epsilon)\cos(\mu) - \sin(\mu)\sin(\epsilon))\sin(g\sin(\Omega t)) \\
&- (\cos(\epsilon)\langle\cos(\mu)\rangle - \sin(\epsilon)\langle\sin(\mu)\rangle)\sin(g\sin(\Omega t))] = 0,
\end{aligned} \tag{11}
$$

where $r_1 = \cos(\mu) - \langle\cos(\mu)\rangle$, $r_2 = \sin(\mu) - \langle\sin(\mu)\rangle$, $r_3 = \cos(\mu) - \langle\cos(\mu)\rangle$, and $r_4 = \sin(\mu) - \langle\sin(\mu)\rangle$.

Simplifying Eq. (11) by using the expressions for the respective averages in Eq. (9), this yields:

$$
\begin{aligned}
&\ddot{\mu} + b_1\dot{\mu} + b_2\dot{\mu}^3 + 3b_2\dot{\mu})^2\dot{\epsilon} + 3b_2\dot{\epsilon})^2\dot{\mu}) \\
&+ \frac{\beta^2[1-\cos(\epsilon)(\cos(\mu) - J_o(\mu_o)) + \sin(\epsilon)\sin(\mu)]^2}{[\sin(\epsilon)(\cos(\mu) - J_o(\mu_o)) + \cos(\epsilon)\sin(\mu)]^3} \\
&- A[\sin(\epsilon)(\cos(\mu)\cos(g\sin(\Omega t)) - J_o(\mu_o)J_o(g)) \\
&+ (\sin(\mu)\cos(\epsilon))\cos(g\sin(\Omega t)) \\
&+ (\sin(\epsilon)\sin(\mu) - \cos(\epsilon)\cos(\mu))\sin(g\sin(\Omega t))] = 0.
\end{aligned} \tag{12}
$$

For small values of g, $\cos(g\sin(\Omega t)) \approx 1$ and $\sin(g\sin(\Omega t)) \approx g\sin(\Omega t)$. By freezing the slow motion variable ϵ and assuming the maximum value of the fast motion μ, we can appropriately write [48],

$$
\ddot{\mu} = G\sin(\Omega t), \tag{13}
$$

where $G = -gA$. The solution to Eq. (13) is given as:

$$
\mu = -\mu_o\sin(\Omega t), \tag{14}
$$

where $\mu_o = \frac{G}{\Omega^2}$. Hence, Eq. (10) becomes,

$$
\begin{aligned}
&\ddot{\epsilon} + b_1\dot{\epsilon} + b_2\dot{\epsilon}^3 + \frac{\beta^2[(1-J_0(\frac{G}{\Omega^2})\cos(\epsilon))^2]}{[J_0(\frac{G}{\Omega^2})\sin(\epsilon)]^3} \\
&- A\left[J_0(g)J_0\left(\frac{G}{\Omega^2}\right)\sin(\epsilon)\right] = f\sin(\omega t).
\end{aligned} \tag{15}
$$

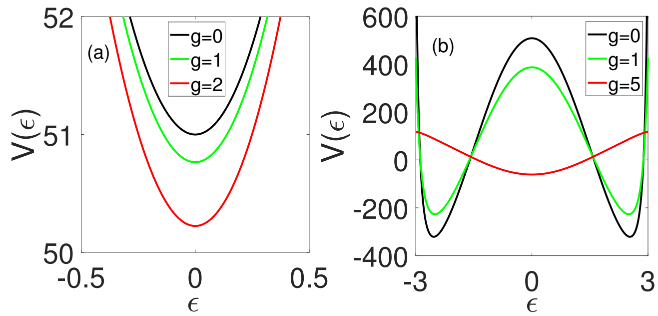

FIG. 5. [Color online] The effective potential Eq. (16) versus ϵ. (a) Single-well potential ($\beta = 10$, $A = 1$, $\Omega = 50$, $t = 1$), showing the impact of phase-modulation from $g = 0$ (zero-phase) to $g = 1$ and $g = 2$. (b) Double-well potential ($\beta = 4$, $A = 500$, $\Omega = 50$, $t = 1$), showing the impact of phase modulation from $g = 0$ (zero-phase) to $g = 1$ and $g = 5$.

Eq. (15) represents the theoretical equation for the slow motion of the gyroscope in terms of ϵ, with the parameters of fast motion acting as a modulating function of the phase of the potential embedded in it. From Eq. (15), we extract the effective potential $V(\epsilon)$ as

$$
V(\epsilon) = \frac{\beta^2 J_0(\frac{G}{\Omega^2})}{(1 + J_0(\frac{G}{\Omega^2})\cos(\epsilon))} + AJ_0\left(\frac{G}{\Omega^2}\right)J_0(g)\cos(\epsilon). \tag{16}
$$

Figure 5 depicts the phase-modulated gyroscope's effective potential, plotted against ϵ at three different modulation amplitudes. For $\beta = 10$, corresponding to the single-well case as shown in Fig. 5(a), the phase-modulation amplitude g increases the depth of the effective potential. Greater external excitation is required to drive the system out of equilibrium or into a neutral state. For $\beta = 4$, corresponding to the double-well case, phase modulation reduces the well depth, thereby driving the system into a free state as shown in Fig. 5(b). In addition, high-amplitude modulation can collapse the double-well structure into a single-well. These results show that the phase modulation is capable of either enhancing or suppressing the system's response depending on the choice of parameters.

Proceeding further, the slow oscillation equation (15) may be approximated around the equilibrium points $(\epsilon^*, \dot{\epsilon}^*)$, where the slow oscillation occurs, employing the approximation $\epsilon^+_{\max(\min)} = 2k\pi$, where k is an integer. The system's motion can be written in terms of the deviation of the slow motion ϵ from the equilibrium positions ϵ^*, defined as $\sigma = \epsilon - \epsilon^*$. This leads to the following equation:

$$
\begin{aligned}
&(\ddot{\sigma}+\ddot{\epsilon^*})+b_1(\dot{\sigma}+\dot{\epsilon^*})+b_2(\dot{\sigma}+\dot{\epsilon^*})^3\\
&+\frac{\beta^2[(1-J_0\left(\frac{G}{\Omega^2}\right)\cos(\sigma+\epsilon^*))^2]}{[J_0(\frac{G}{\Omega^2})\sin(\sigma+\epsilon^*)]^3}\\
&-A[J_0(g)J_0\left(\frac{G}{\Omega^2}\right)\sin(\sigma+\epsilon^*)]=f\sin(\omega t),
\end{aligned}
\tag{17}
$$

which can be expressed further as:

$$
\begin{aligned}
&\ddot{\sigma}+\ddot{\epsilon^*}+b_1\dot{\sigma}+b_1\dot{\epsilon^*}+b_2\dot{\sigma}^3+3b_2\dot{\sigma}^2\dot{\epsilon^*}+3b_2\dot{\sigma}\dot{\epsilon^*}^2+b_2\dot{\epsilon}^3\\
&+\frac{\beta^2[(1-J_0\left(\frac{G}{\Omega^2}\right)\cos(\sigma)\cos(\epsilon^*)+J_0(\frac{G}{\Omega^2})\sin(\sigma)\sin(\epsilon^*))^2]}{[J_0(\frac{G}{\Omega^2})(\sin(\sigma)\cos(\epsilon^*)+\sin(\epsilon^*)\cos(\sigma))]^3}\\
&-A[J_0(g)J_0\left(\frac{G}{\Omega^2}\right)(\sin(\sigma)\cos(\epsilon^*)+\sin(\epsilon^*)\cos(\sigma))]\\
&=f\sin(\omega t).
\end{aligned}
\tag{18}
$$

Considering only small deviations from the equilibrium points, then $\sin(\sigma)\approx\sigma$ and $\cos(\sigma)\approx 1$. For $J_0(\frac{G}{\Omega^2})>0,(<0)$, then $\epsilon^*=\epsilon^*_{\max(\min)}$. Therefore, $J_0(\frac{G}{\Omega^2})\cos(\epsilon^*)=\left|J_0(\frac{G}{\Omega^2})\right|$ and Eq. (18) reduces to;

$$
\begin{aligned}
&\ddot{\sigma}+(b_1+3b_2\dot{\epsilon^*}^2)\dot{\sigma}+b_2\dot{\sigma}^3+3b_2\dot{\sigma}^2\dot{\epsilon^*}\\
&+\frac{\beta^2\left[(1-\left|J_0(\frac{G}{\Omega^2})\right|)^2\right]}{[|J_0(\frac{G}{\Omega^2})|\sigma]^3}\\
&-A\left[J_0(g)\left|J_0\left(\frac{G}{\Omega^2}\right)\right|\sigma\right]\\
&\quad=f\sin(\omega t).
\end{aligned}
\tag{19}
$$

Dropping the nonlinear terms in Eq. (19), we obtain

$$
\ddot{\sigma}+\lambda\dot{\sigma}+\omega_r^2\sigma=f\sin(\omega t), \tag{20}
$$

where

$$
\omega_r^2=AJ_0(g)\left|J_0(\frac{gA}{\Omega^2})\right| \tag{21}
$$

is the resonant frequency, and $\lambda=(b_1+3b_2\epsilon^{*2})$ is the damping coefficient. At the trivial equilibrium point ($\epsilon^*=0$), the damping coefficient reduces to b_1 .

Equation (20) is the approximate theoretical equation from which the amplitude of the response Q, of the system to the HF phase modulation of the potential function, can be obtained. We solved Eq. (20) by assuming a sinusoidal solution in the form: $\sigma(t)=A_m\sin(\omega t+\theta)$. Then, by substituting $\sigma(t)$, $\dot{\sigma}(t)$, and $\ddot{\sigma}(t)$ into the equation, and using the relevant trigonometric identities, the equation was simplified, and the coefficients of $\sin(\omega t)$ and $\cos(\omega t)$ were equated separately to obtain an expression for the amplitude. This yielded the steady-state solution corresponding to Eq. (20) as $\sigma(t)=K_m\sin(\omega t+\theta)$, with $\theta=\tan^{-1}\left(-\frac{\lambda\omega}{\omega_r^2-\omega^2}\right)$ and $K_m=\frac{f}{\sqrt{S}}$, where $S=(\omega_r^2-\omega^2)^2+\lambda^2\omega^2$ and $\eta=\omega_r^2-\omega^2$. $\sigma(t)$ describes the system's dynamics in the long time limit $t\to\infty$. The response amplitude is denoted by the quantity Q. It is the ratio of the amplitude of $\sigma(t)$, K_m to the LF signal's amplitude, f. That is,

$$
Q=\frac{K_m}{f}=\frac{1}{\sqrt{S}}. \tag{22}
$$

In Eq. (22), Q is maximum when S is minimum, i.e., at resonance $\omega_r=\omega$ or $\eta=0$, provided the frequency ω is fixed. In the case when ω is varied, a separate condition can be obtained. By assuming that a system parameter (say μ) is varied, the parameter value at which resonance occurs, herein denoted as μ_{vr}, can be computed from the roots of the equation $S^1_\mu=\frac{dS}{d\mu}=0$ and $S^2_{\mu|\mu=\mu_{vr}}>0$. Using the expression for S, the frequency value ω_{vr} must therefore satisfy the condition $S_\omega=2\lambda^2\omega-4\omega(\omega_r^2-\omega^2)=0$, so that

$$
\omega=\omega_{vr}=\sqrt{\omega_r^2-\frac{\lambda^2}{2}}. \tag{23}
$$

Having established the theoretical conditions for VR in this case, we now demonstrate the occurrence of VR and its enhancement and suppression numerically, by variation of the phase modulation parameter. The response was computed from the amplitudes Q_s and Q_c of the Fourier spectrum of the output signal, where Q_s and Q_c are defined by [7]:

$$
\begin{aligned}
Q_s&=\frac{2}{nT}\int_0^{nT}\phi(t)\sin(\omega t)dt\\
Q_c&=\frac{2}{nT}\int_0^{nT}\phi(t)\cos(\omega t)dt.
\end{aligned}
\tag{24}
$$

The system's amplitude is given by,

$$
A=\sqrt{Q_s^2+Q_c^2}. \tag{25}
$$

The system's amplitude of response to the LF signal is thus given as

$$
Q=\frac{A}{f}=\frac{\sqrt{Q_s^2+Q_c^2}}{f}. \tag{26}
$$

The frequency-response curve provides useful information about how a system's output evolves as the frequency of the input varies [63]. It is an efficient tool for predicting the system's evolution under different constraints, and finds useful applications in a wide range of disciplines. For instance, there are several practical applications in relation to coupled oscillators [64], and in plasma physics [65]. Figure 6 depicts the low frequency-response curve, i.e. Q against ω, plotted using the analytically obtained Q from Eq. (22) and comparing with the numerically calculated Q from Eq. (26) as a function of

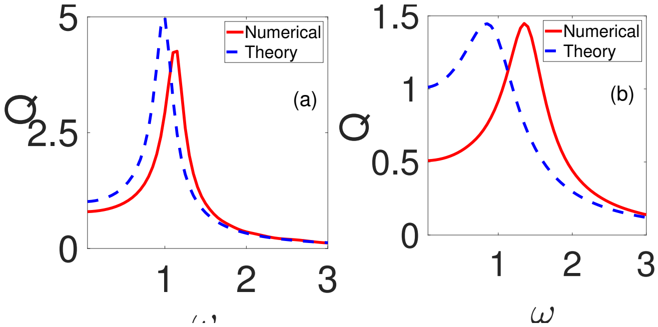

FIG. 6. [Color online] Comparison between the theoretical Q (Eq. (22)) and the numerically computed Q (Eq. 26). Each is plotted against ω using the parameters: $b_1 = 0.5$, $b_2 = 0.05$, $\Omega = 70$, $\lambda = 0.7$. (a) Single-well potential with $A = 1$, $\beta = 3$, $f = 1$ for $g = 0.2$. (b) Double-well potential with $A = 1$, $\beta = 1$, $f = 0.05$, for $g = 0.2$.

the low-frequency, ω, setting the simulation parameters as $b_1 = 0.5$, $b_2 = 0.05$, $\Omega = 70$, and $\lambda = 0.7$. Figure 6(a) represents the single-well case with $\beta = 10$, $A = 1$, and $f = 1$, while Fig. 6(b) represents the double-well case with $\beta = 1$, $f = 0.05$, and $A = 1$. In both instances the phase-modulation amplitude, $g = 0.2$. The results are in good agreement, and particularly notable when $\omega > 5$ for the single-well and when $\omega > 1.0$ for the double-well. The disparity at low frequencies of the response curves could be attributed to approximations employed in the theoretical analysis. The theoretical solutions rely on the linear approximations in which higher-order terms in the nonlinear systems were neglected (as done between Eqs. (18) and (19)). Thus, at low frequencies, nonlinear effects might dominate, leading to deviation of theory from the numerical solutions, thereby rendering analytical solutions more difficult in tracking the numerical results and less accurate. Many perturbation methods such as direct separation of motions, assume small deviations from equilibrium. The system might explore larger nonlinear effects at low frequencies, which could invalidate the assumptions. While our numerical method has accurately accounted for these deviations, the analytic approach might not [66].

In addition to the agreement between theory and numerical Q shown in Figure 6, we find that the derived resonance frequency ω_r, given in Eq. (21) predicted the values of g at which resonance occurs. This is illustrated in Figure 7 in which we presented the theoretical Q and ω_r both plotted against g, for the single-well and double-well cases. In the single-well case, Fig. 7(a) shows the Q peaks at frequency of $\omega = \omega_r = 0.5$. The first resonance peak, $Q_{\max 1}$, occurs at $g = 1.95$, while two subsequent peaks, $Q_{\max 2,3}$ indicated by the vertical dashed lines, appear at $g = 6.45$ and $g = 7.7$, respectively. The g values for the three peaks shown in Fig. 7(a) are clearly captured by Fig. 7(b) illustrating the variation of ω_r with g. The vertical dashed lines in Fig. 7(b) have been drawn from the points where the horizontal dashed line at $\omega = 0.5$

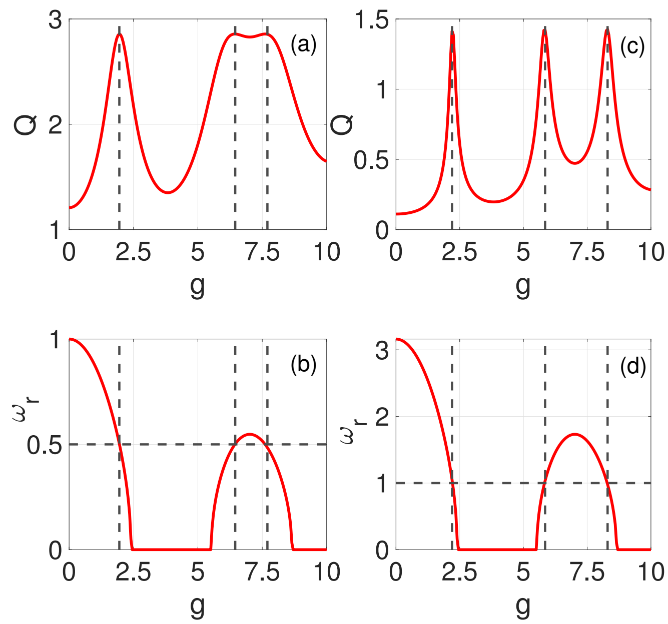

FIG. 7. [Color online] Plots of theoretical Q versus g for and ω_r ($\omega_r^2 = AJ_0(g)|J_0(\frac{gA}{\Omega^2})|$) versus g. Panels (a) Q vs g and (b) ω_r vs g for the single-well case with $\omega = 0.5$, $A = 1$, $\beta = 3$, and $f = 0.5$. The horizontal dashed line represents $\omega_r = \omega = 0.5$. Panels (c) Q vs g and (d) ω_r vs g are for the double-well case with $\omega = 1$, $A = 1$, $\beta = 1$, and $f = 0.05$. The horizontal dashed line represents $\omega_r = \omega = 1$. In (a)-(d), the vertical dashed lines represent the values of ω_r and g at which Q is maximal. Other parameters are: $b_1 = 0.5$, $b_2 = 0.05$, $\Omega = 50\omega$, and $\lambda = 0.7$.

intersects the ω_r vs g curve, thereby predicting the occurrence of peaks in Fig. 7(a) when $\omega_r = \omega$. Specifically, two resonance peaks exist for $0 < \omega \leq 0.546$, but for $0.546 < \omega \leq 1.0$, only a single resonance peak is observed. Thus, the number of peaks depends on the low-frequency (ω) range under consideration.

For the double-well case, Figures 7(c) and (d) show the theoretical Q and ω_r, both plotted against g. With the low-frequency fixed at $\omega = \omega_r = 1.0$ in Fig. 7(c), the first resonance peak, $Q_{\max 1}$, occurred at $g = 2.2$, followed by two additional peaks, $Q_{\max 1,2}$, at $g = 5.85$ and $g = 8.3$, respectively. These resonance g value locations are marked by vertical dashed lines. It can be seen that the corresponding ω_r vs g plot shown in Figure 7(d) predicted the g values at which resonance occur. The vertical dashed lines from the intersections of the horizontal dashed line at $\omega = 1.0$ of the ω_r-g curve align exactly with the Q plot shown in Figure 7(c). Similarly to the single-well case, the number of peaks depends on the range of ω. Three peaks can be observed for $0 < \omega \leq 1.73$, while only a single peak exists for $\omega > 1.73$.

Thus, Figures 7 is indicative of resonance induced by frequency matching ($\omega_r = \omega$) in both the single-well and double-well case. The relationship between Q and ω_r is crucial for predicting and optimizing the performance and stability of the gyroscope system.

We now proceed to provide clear evidences of resonance suppression and enhancement by time-periodic phase modulation. Figure 8 depicts the frequency-response curve for both the single-well (Figure 8(a)) and the double-well (Figure 8(b)) parameter settings for increasing values of the phase-modulation amplitude, g. In the single-well case, there is a single peak over the frequency range examined herein. The presence of phase modulation weakly suppresses the response Q which implies that the zero-phase ($g \approx 0$) gives the maximum response at the lowest value of $\omega \approx 5$ as shown in Fig. 8(a). Suppression occurs for $0 < g < 5$. For $g > 5$, the response is weakly enhanced. In the double-well case, on the other hand, multiple peaks can appear over a wider frequency range. However, the first peak appearing in the weak frequency regime is dominant in magnitude - its magnitude being 1000 times the magnitudes of the other peaks observed at higher frequency regimes. Here, phase modulation significantly enhances the primary resonance even at higher ω values where multiple peaks occur as shown in the inset. The zero-phase case (depicted by grey color) in Fig. 8(b) evidently shows the least response Q peak appearing at the resonance frequency of $\omega \approx$ 1.35, 55, 81, 119 and 189. On the other hand, the non-zero-phase cases depicted by brown, blue and green clearly exhibits enhanced response for all ω regimes where resonance occurred. In lower frequency regime, typically $g < 2$, the resonant frequency decreases correspondingly as the amplitude of phase modulation increases. In the double-well case, resonance peaks occurred over a wider range of values of ω, providing a more complete picture of a system's behaviour [67].

Figures 9(a) and (b) illustrate the response of the system as a function of g, the amplitude of the phase-modulating function for different values of f, the amplitude of the low-frequency time-periodic external force for both the single-well and double-well cases, respectively. In the single-well case, suppressed multiple resonances were observed as f increased from f=0.5,2, 2.5, 3,4, to 5. In the double-well case, anti-resonance, resonance suppression and enhancement are evident as the amplitude f increased progressively. Specifically in the weak amplitude ($0 \leq g < 2$) of Fig. 9(b), resonance suppression takes place with intermittent anti-resonance at f = 3 and 5; while for higher amplitudes ($2 \leq g \leq 20$) resonance enhancement precedes resonance suppression. Resonance peaks occurred at multiple values of g in both cases - which is consistent with our theoretical predictions. For the single-well, three peaks occurred at $g \approx 7, 13.4$ 19.6 in addition to the primary resonance at $g = 0$; while for the double-well the peaks occurred at $g \approx 0.8, 3.8, 10.2$ and 16.6. The suppression and enhancement scenarios implies that time-periodic phase-modulation can be employed to control the vibrational modes of a gyroscope, which can potentially be useful in the gyroscope applications enumerated in Ref. [68].

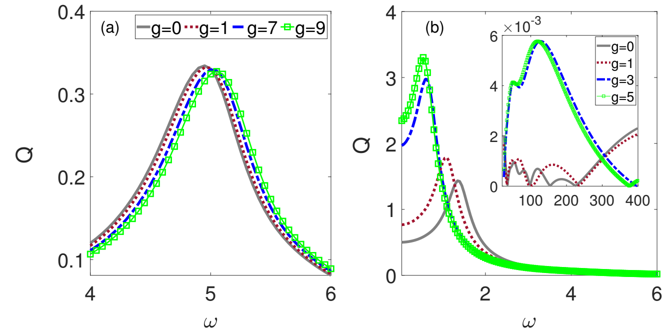

FIG. 8. [Color online] Frequency-response curve of the system solution given by Eq. (26) when modulated by a high-frequency time-periodic force for different amplitudes of the gyroscope's phase. (a) Single-well case with $A = 1$, $\beta = 10$, $f = 1$, for $g = 0, 1, 7$ and 9. (b) Double-well case with $A = 1$, $\beta = 1$, $f = 0.05$, for $g = 0, 1, 3$ and 5. The inset in (b) indicates the resonance enhancement at extremely high ω-values. The other parameter values were $b_1 = 0.5$, $b_2 = 0.05$, $\Omega = 70$.

B. Case 2: $\Gamma_m(t) = f\sin(\omega t)$, $\Gamma_f(t) = g\sin(\Omega t)$

We now examine the scenario where a low-frequency force $\Gamma_m(t) = f\sin(\omega t)$ modulates the gyroscope's phase and a high-frequency force $g\sin(\Omega t)$ acts as an additive external drive. With all variables retaining their definitions, the equation of motion becomes:

$$\ddot{\phi} + b_1\dot{\phi} + b_2\dot{\phi}^3 + \beta^2\left(\frac{(1-\cos\phi)^2}{\sin(\phi)^3}\right) - A\sin(\phi - f\sin(\omega t)) = g\sin(\Omega t), \tag{27}$$

The associated potential for Eq. (27) is given as:

$$V(\phi, t) = \frac{\beta^2}{(1+\cos\phi)} + A\cos(\phi - f\sin(\omega t)). \tag{28}$$

Proceeding as in Case 1 of section III A, the slow motion equation for the dynamics (Eq. (27)) is given as:

$$\begin{aligned} &\ddot{\epsilon} + b_1\dot{\epsilon} + b_2\dot{\epsilon}^3 + \frac{\beta^2[(1 - J_0\left(\frac{-g}{\Omega^2}\right)\cos(\epsilon))^2]}{\left[J_0\left(\frac{-g}{\Omega^2}\right)\sin(\epsilon)\right]^3} \\ &- A[J_0\left(\frac{-g}{\Omega^2}\right)\sin(\epsilon)\cos(f\sin(\omega t)) \\ &+ J_0\left(\frac{-g}{\Omega^2}\right)\cos(\epsilon)\sin(f\sin(\omega t))] = 0. \end{aligned} \tag{29}$$

For small values of f, $\cos(f\sin(\omega t)) \approx 1$ and $\sin(f\sin(\omega t)) \approx \sin(\omega t)$. Therefore, Eq. (29) becomes:

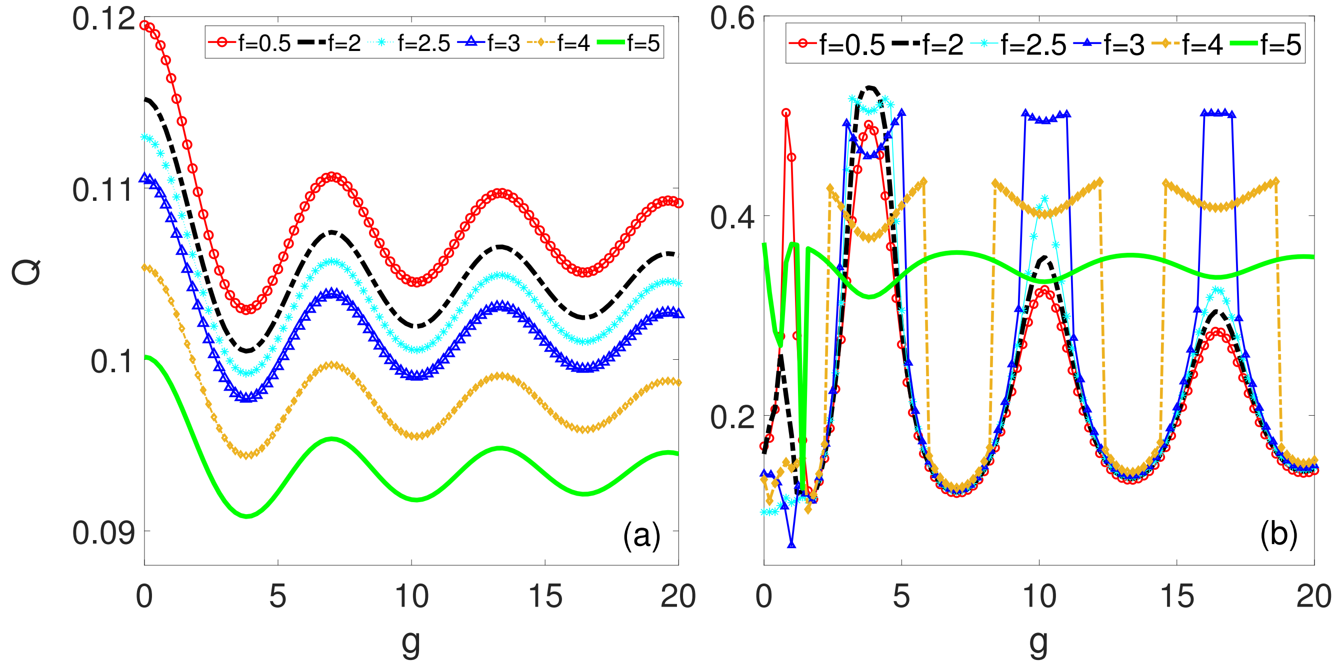

FIG. 9. [Color online] Response amplitude of the system solution Eq. (26) versus g showing evidence of resonance suppression when modulated by a high-frequency time-periodic force, for different values of the amplitude f of the external drive. (a) Single-well case with $A = 1$, $\beta = 10$ for $f = 0.05, 0.5$ and 2. (b) Double-well case with $A = 10$, $\beta = 4$ for $f = 0.5, 2$ and 2.5. The other parameters were $b_1 = 0.6$, $b_2 = 0.004$, $f = 0.05$, $\omega = 0.5$, $\Omega = 50$.

$$\begin{aligned}&\ddot{\epsilon} + b_1\dot{\epsilon} + b_2\dot{\epsilon}^3 + \frac{\beta^2[(1 - J_0\left(\frac{-g}{\Omega^2}\right)\cos(\epsilon))^2]}{[J_0\left(\frac{-g}{\Omega^2}\right)\sin(\epsilon)]^3}\\ &- A[J_0\left(\frac{-g}{\Omega^2}\right)\sin(\epsilon)\\ &+ J_0\left(\frac{-g}{\Omega^2}\right)\cos(\epsilon)f\sin(\omega t)] = 0.\end{aligned} \tag{30}$$

The effective potential, $V_{eff}(\epsilon)$ can be extracted as:

$$\begin{aligned}V(\epsilon) &= \frac{\beta^2 J_0(\frac{-g}{\Omega^2})}{(1 + J_0(\frac{-g}{\Omega^2})\cos(\epsilon))}\\ &+ AJ_0\left(\frac{-g}{\Omega^2}\right)[\cos(\epsilon) + \sin(\epsilon)f\sin(\omega t)].\end{aligned} \tag{31}$$

Proceeding as before, we reduce the equation of motion to that of linearly damped driven oscillator:

$$\ddot{\sigma} + \lambda\dot{\sigma} + \omega_r^2\sigma = F\sin(\omega t), \tag{32}$$

where

$$\omega_r^2 = A\left|J_0\left(\frac{g}{\Omega^2}\right)\right| \tag{33}$$

is the resonant frequency, $F = A\left|J_0(\frac{g}{\Omega^2})\right| f$ and $\lambda = (b_1 + 3b_2\dot{\epsilon}^{*2}$, the damping coefficient. At the zero equilibrium, $\epsilon^{*2} = 0$, $\lambda = b_1$. The steady-state solution $\sigma(t) = K_m\sin(\omega t + \theta)$ corresponding to Eq. (32) describes a system similar to Case 1 and, in the long time limit, $t \to \infty$ with $K_m = \frac{F}{\sqrt{S}}$. Here, $S = [(\omega_r^2 - \omega^2)^2 + \lambda^2\omega^2]$, and $\eta = \omega_r^2 - \omega^2$. The response amplitude is denoted by the quantity Q, and defined as:

$$Q = \frac{K_m}{F} = \frac{1}{\sqrt{S}}. \tag{34}$$

In Eq. (34), Q is maximum when S is minimum, i.e. at resonance when $\omega_r = \omega$ or $\eta = 0$. Analogous to *Case 1*, the condition given by Eq. (23) when ω is varied holds, with ω_r now defined by Eq. (33).

Figure 10 depicts the theoretically calculated Q and the equivalent ω_r given by Eq. (33), both plotted against g, for this case, where a low-frequency force modulates the phase of the oscillator driven by high-frequency external excitation for the single-well and double-well configurations. For the single-well parameter setting, Figure 10(a) shows the resonance peaks in Q when the frequency $\omega = \omega_r = 0.5$. The first resonance peak, $Q_{\max 1}$, occurs at $g = 1225$, while subsequent peaks, $Q_{\max 2,3,4,5}$, appear at $g = 1850$, $g = 2975$, $g = 4000$, and $g = 4800$, as marked by the vertical dashed lines. The variation of ω_r with g is displayed in Figure 10(b), with the vertical dashed lines drawn from the points where the horizontal dashed line at $\omega = 0.5$ intersects the ω_r vs g plot, indicating that resonance peaks occur when $\omega_r = \omega$, and

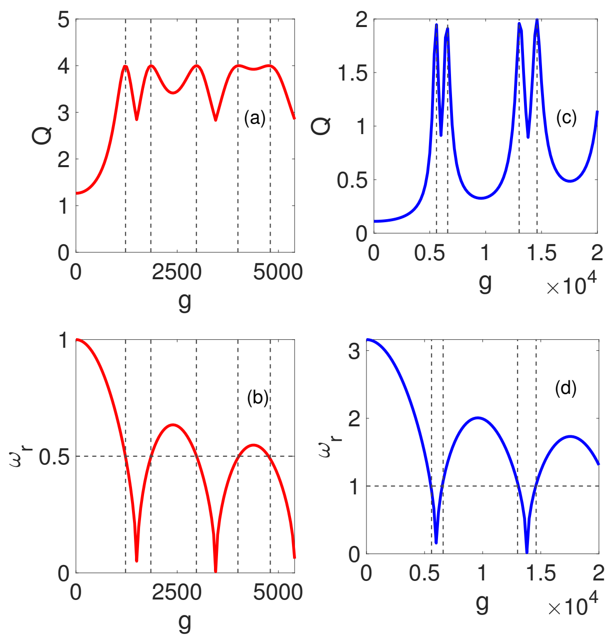

FIG. 10. [Color online] Plots of theoretical Q versus g and ω_r ($\omega_r^2 = A|J_0(\frac{g}{\Omega^2})|$) versus g of a phase-modulated gyroscope oscillator. $b_1 = 0.5$, $b_2 = 0.05$, $\Omega = 50\omega$, $\lambda = 0.5$, $f = 0.5$. (a) and (b) Single-well with $\omega = 0.5$, $A = 10$,$\beta = 1$. The horizontal dashed line represents $\omega_r = \omega = 0.5$ (c) and (d) Double-well with $\omega = 1$, $A = 1$, $\beta = 1$. Horizontal dashed line represents $\omega_r = \omega = 1$. The vertical dashed lines represent the values of ω_r and g at which Q becomes maximum.

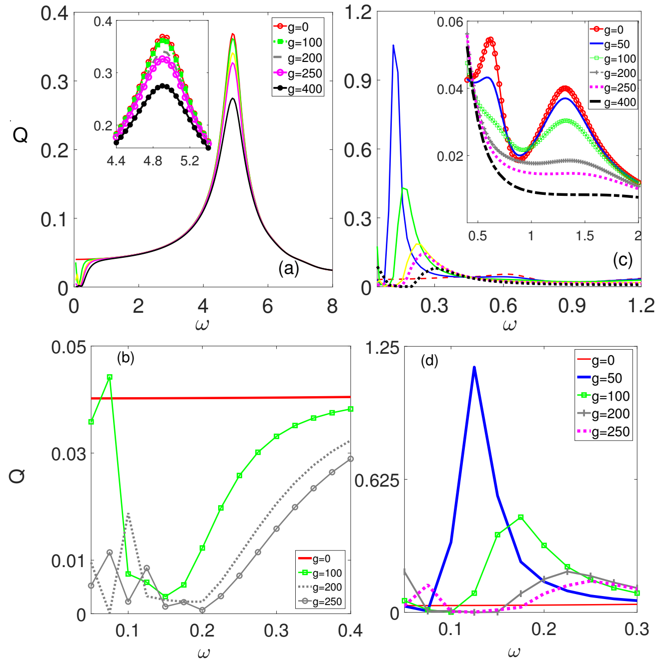

FIG. 11. [Color online] Frequency response curve of the system solution (34) showing resonance suppression when modulated by a low-frequency, time-periodic, force for different values of the amplitude g of the external drive, with parameters $b_1 = 0.5$, $b_2 = 0.05$, $f = 0.5$, $\Omega = 50\omega$. (a) and (b) Single-well case with $A = 1$, $\beta = 10$, for g=0,100, 200, 250 and 400. The inset in (a) shows the frequency suppression domain; while panel (b) shows the weak frequency suppression domain. (c) and (d) Double-well case with $A = 1$, $\beta = 1$, for g=0, 50, 100, 200, 250, and 400. The inset in (c) shows a zoom of the higher frequency suppression domain; while panel (d) shows the weak frequency suppression domain.

showing that, in the single-well case, resonance occurs due to frequency matching ($\omega_r = \omega$). In particular, five resonance peaks exist for $0 < \omega \leq 0.63$ but, for $0.63 < \omega \leq 1.0$, only a single resonance peak is observed.

For the double-well case, Figures 10(c) and (d) show the theoretical Q and the corresponding ω_r versus g curves. With $\omega = \omega_r = 1.0$ in Figure 10(c), the first resonance peak, $Q_{\max 1}$, appears at $g = 2.2$, followed by two additional peaks, $Q_{\max 1,2}$, at $g = 5600$, $g = 6600$, $g = 13000$ and $g = 14600$. These resonance points are indicated by the vertical dashed lines. The corresponding ω_r vs g curve shown in Figure 10(d) further confirms that the vertical dashed lines from the intersections of the horizontal dashed line at $\omega = 1.0$ with the ω_r-g curve align with the peaks in Figure 10(c). Furthermore, the number of peaks depends on the range of ω: four peaks are present for $0 < \omega \leq 2.01$, while only a single peak exists for $\omega > 2.01$.

We now show evidence of VR suppression in this case. The response amplitudes Q against the low-frequency, ω for different values of the external drive amplitude g are as shown in Fig. 11 for both the single-well and double-well settings. Here, $f = 0.5$ - the amplitude of the time-periodic phase-modulating low-frequency force is fixed. For the single-well case shown in Fig. 11(a), the primary resonance due to time-periodic phase-modulation ($f \sin(\omega t)$) was observed for $g = 0$ with $f = 0.5$. For the other higher external drive amplitudes (g =100, 200, 250), resonance suppression appeared. We have used even higher values of g, up to 250, to distinguish between consecutive curves. On the contrary, in Fig. 11(b), a double primary resonance peak was found in the double-well case with zero-phase excitation ($g = 0$): one within the frequency range of ω ($0.5 \leq \omega \leq 0.8$), while the second peak occurred in the neighbourhood of ω ($1 \leq \omega \leq 1.7$). By turning on the phase excitation with increased amplitude g (i.e. 50 to 250), resonance suppression is activated. First, at g slightly greater than zero ($5 \leqslant g \leqslant 50$), three resonance peaks first appear, with one giant peak in the low frequency regime. However, there is gradual elimination of the enhanced first peak located in the frequency bandwidth: $0.5 \leq \omega \leq 0.8$, as g increases progressively. The appearance of double resonance is consistent with the theoretical prediction of multiple resonance peaks presented in Fig. 10(d) within this ω range.

The response amplitudes in Fig. 11(c) are far greater than those observed in the single-well case in Fig. 11(a). In the single-well case shown in Fig. 11(a), the frequencies at which resonances occurred are close and narrower than the distinct frequency bandwidths observed in Fig. 11(b).

This occurred for a single-well at $\omega \approx 5$. As the amplitude, g increases from 0 to 250 in each case, there is a corresponding decrease in the response amplitude, Q. Figure 11(b) shows a zoom of the system's response in the lower frequency domain ($0 < \omega \leqslant 0.4$) of Fig. 11(a). In this low frequency regime, the oscillator is in its quiescent state in the absence of the modulating force ($g = 0$). Evidently, the activation of the time-periodic phase excitation *induced-antiresonance* as its amplitude, g increased from 0 to 250 as shown in Fig. 11(a) for the single-well case. However, in the double-well case illustrated in (d), giant VR is first induced at $\omega \approx 0.1$ when the excitation amplitude is $g = 50$. This is followed, however, by the occurrence of VR suppression at slightly higher resonance frequencies as g increases further to 250.

Thus it is evident that, by modulating the phase of an oscillatory mechanical system with a low-frequency time-periodic force, the system's response can be either enhanced or suppressed in different parameter regimes. In cases where the phase of the oscillator is accessible, phase modulation would be a useful technique for effecting vibration control in engineering systems when high-amplitude vibrations are undesirable. Notably, in previous studies, negative resistance electromagnetic shunt dampers were used to reduce vibrations in high-temperature superconducting maglev systems [69]; while inertial nonlinear energy sinks (NESs) installed at the boundaries of an elastic beam were used to suppress its transverse multi-modal resonances [70, 71], and there are many other similar examples.

IV. CONCLUDING REMARKS

In examining the response of a driven gyroscope to time-periodic phase-modulation, we have used a stability analysis in the absence of external forces to show that the system's equilibrium points are controlled by the amplitude, A, of the periodic component of the potential, and β, the parameter of the aperiodic component. With β treated as the bifurcation parameter, the system experiences a pitchfork bifurcation at $\beta = 2\sqrt{A}$ at which it undergoes a transition from a single-well to a double-well potential state. In the presence of a high-frequency time-periodic phase-modulating force, the trivial equilibrium $\phi_1^* = 0$ changes, so that the phase-modulation parameters cooperate with β and A to induce complex dynamics. Within the framework of vibrational resonance (VR), where the presence and characteristics of a high-frequency driving force can be exploited to maximize the response of an oscillator to a low-frequency drive, we investigated the response of the phase-driven gyroscope oscillator, both theoretically and numerically, based on two scenarios. In the first case, the gyroscope phase was modulated by a high-frequency time-periodic force $f\sin(\Omega t)$, while externally driven by a low-frequency force $g\sin(\omega t)$. In the second case, the gyroscope's phase was modulated by a low-frequency time-periodic force $f\sin(\omega t)$, while externally driven by high-frequency force $g\sin(\Omega t)$. In the former case, time-periodic phase-modulation promotes multiple resonance enhancement over resonance suppression for appropriate choices of parameters. In the latter case, time-periodic phase-modulation induces giant VR and anti-resonances, as well as promotes VR suppression over enhancement, for appropriate choice of the phase modulation parameters. The response enhancement and suppression have a range of potential applications in different disciplines. In aerodynamics, for instance, vibrational response suppression in aircraft wings can aid aerodynamic efficiency and structural safety [68, 72]. It can be utilized to prevent flutter and improve flight stability. In addition, vibrational response suppression in gyroscope systems may find application in space structures for satellite orientation control [73–75], and could also be beneficial to wind turbines through the reduction of mechanical stress [76]. On the other hand, regimes of enhanced vibrational response in a gyroscope could, in certain circumstances, signal structural flaws or instabilities that should be avoided [77]. On the contrary, automotive gyroscopes use enhanced responses for providing improved stability [78]. Response enhancement is also utilized in earthquake detection for early warning systems and in consumer electronics to improve interface responsiveness, with electrostatic transduction being a common method due to its low power requirement and fast response [79]. These applications highlight the adaptability of driven gyroscopes for technological advancement, seismology, renewable energy, and space exploration.

ACKNOWLEDGMENTS

We thank the reviewers for their insightful, constructive stimulating comments.

[1] V. M. N. Passaro, A. Cuccovillo, L. Vaiani, M. De Carlo, and C. E. Campanella, Gyroscope technology and applications: A review in the industrial perspective, Sensors **17**, 2284 (2017).

[2] J. Fang and J. Qin, Advances in atomic gyroscopes: A view from inertial navigation applications, Sensors **12**, 6331 (2012).

[3] R. Goyal, M. Chen, M. Majji, and R. E. Skelton, Gyroscopic tensegrity robots, IEEE Robot. Autom. Lett. **5**, 1239 (2020).

[4] R. Usubamatov, Mathematical model for gyroscope effects, in *AIP Conference Proceedings*, Vol. 1660 (AIP Publishing, 2015) p. 02209.

[5] M. D. Ardema, *Analytical Dynamics: Theory and Applications* (Springer Science & Business Media, 2006).

[6] M. N. Armenise, C. Ciminelli, F. Dell'Olio, and V. M. Passaro, *Advances in Gyroscope Technologies* (Springer Science & Business Media, 2011).

[7] P. S. Landa and P. V. E. McClintock, Vibrational resonance, J. Phys. A: Math. & Gen. **33**, L433 (2000).

[8] S. Rajasekar and M. A. F. Sanjuán, *Nonlinear Resonances*, 1st ed. (Springer Series in Synergetics, Switzerland, 2016).

[9] U. E. Vincent, P. V. E. McClintock, I. A. Khovanov, and S. Rajasekar, Vibrational and stochastic resonances in driven nonlinear systems, Phil. Trans. Roy. Soc. A **379**, 20200226 (2021).

[10] J. Yang, S. Rajasekar, and M. A. F. Sanjuán, Vibrational resonance: A review, Phys. Rep. **1067**, 1 (2024).

[11] R. Benzi, A. Sutera, and A. Vulpiani, The mechanism of stochastic resonance, J. Phys. A: Math. & Gen. **14**, L453 (1981).

[12] M. I. Dykman, D. G. Luchinsky, R. Mannella, P. V. E. McClintock, N. D. Stein, and N. G. Stocks, Stochastic resonance in perspective, Nuovo Cimento D **17**, 661 (1995).

[13] Y. G. Leng, T. Y. Wang, Y. Guo, Y. G. Xu, and S. B. Fan, Engineering signal processing based on bistable stochastic resonance, Mech. Syst. Signal Process **21**, 138 (2007).

[14] Y. Pan, F. Duan, F. Chapeau-Blondeau, L. Xu, and D. Abbott, Study of vibrational resonance in nonlinear signal processing, Phil. Trans. R. Soc. A **379**, 20200235 (2021).

[15] Z.-X. Zhou, K.-L. Yang, C.-J. Wang, B. Yu, X.-B. Li, and Y.-W. Su, Theory and numerics of vibrational resonance in a three-level atomic optical bistable system, Chaos Solit. Fractals **170**, 113355 (2023).

[16] Y. Wang, P. Wan, Q. Deng, and Y. Fu, Application of stochastic resonance of the single-mode nonlinear optical system in spectrum sensing of cognitive radio networks, Telkomnika **13**, 494 (2015).

[17] B. Xu, Z.-P. Jiang, X. Wu, and D. W. Repperger, Theoretical analysis of image processing using parameter-tuning stochastic resonance technique, in *2007 American Control Conference* (IEEE, 2007) pp. 1747–1752.

[18] B. Wang, Y. Lv, J. Bhola, V. Mahor, R. Yadav, and K. Kaliyaperumal, Vibration compensation for railway track displacement monitoring system using biomedical image processing concept, J. Eng. **2022**, 1076 (2022).

[19] K. Murali, S. Rajasekar, M. V. Aravind, V. Kohar, W. Ditto, and S. Sinha, Construction of logic gates exploiting resonance phenomena in nonlinear systems, Phil. Trans. R. Soc. A **379**, 20200238 (2021).

[20] G.-C. Lizeth, T. Asai, and M. Motomura, Application of nonlinear systems for designing low-power logic gates based on stochastic resonance, IEICE Trans. Inf. & Syst. **5**, 445 (2014).

[21] R. Zheng, K. Nakano, H. Hu, D. Su, and M. P. Cartmell, An application of stochastic resonance for energy harvesting in a bistable vibrating system, J. Sound Vib. **333**, 2568 (2014).

[22] M. Coccolo, G. Litak, J. M. Seoane, and M. A. F. Sanjuán, Energy harvesting enhancement by vibrational resonance, Int. J. Bifurc. Chaos **24**, 1430019 (2014).

[23] Q. Ma, D. Huang, and J. Yang, Adaptive stochastic resonance in second-order system with general scale transformation for weak feature extraction and its application in bearing fault diagnosis, Fluct. Noise. Lett. **17**, 1850009 (2018).

[24] J. Gao, J. Yang, D. Huang, H. Liu, and S. Liu, Experimental application of vibrational resonance on bearing fault diagnosis, J. Braz. Soc. Mech. Sci. Eng. **41**, 1 (2019).

[25] S. Lu, Q. He, and J. Wang, A review of stochastic resonance in rotating machine fault detection, Mech. Syst. Signal Process **116**, 230 (2019).

[26] O. I. Olusola, O. P. Shomotun, U. E. Vincent, and P. V. E. McClintock, Quantum vibrational resonance in a dual-frequency driven Tietz-Hua quantum well, Phys. Rev. E **101**, 052216 (2020).

[27] O. G. Abamba, O. T. Kolebaje, U. E. Vincent, and P. V. E. McClintock, Vibrational resonance in bichromatically excited diatomic molecules in a shifted molecular potential, Phys. Rev. E **110**, 034209 (2024).

[28] K. S. Oyeleke, O. I. Olusola, U. E. Vincent, D. Ghosh, and P. V. E. McClintock, Parametric vibrational resonance in a gyroscope driven by dual-frequency forces, Phys. Lett. A **387**, 127040 (2021).

[29] P. G. Savage, Blazing gyros: The evolution of strapdown inertial navigation technology for aircraft, J. Guid. Control Dyn. **36**, 637 (2013).

[30] T. Roy-Layinde, U. Vincent, S. A. Abolade, O. O. Popoola, J. A. Laoye, and P. V. E. McClintock, Vibrational resonances in driven oscillators with position-dependent mass, Phil. Trans. Roy. Soc. A **379**, 20200227 (2021).

[31] U. E. Vincent, T. O. Roy-Layinde, O. O. Popoola, P. O. Adesina, and P. V. E. McClintock, Vibrational resonance in an oscillator with an asymmetrical deformable potential, Phys. Rev. E **98**, 062203 (2018).

[32] L. Ning and K. Zhao, Vibrational resonance and bifurcation in a fractional order quintic system with distributed time delay, Phys. Scr. **97**, 055205 (2022).

[33] K. S. Oyeleke, O. I. Olusola, O. T. Kolebaje, U. E. Vincent, A. B. Adeloye, and P. V. E. McClintock, Novel bursting oscillations in a nonlinear gyroscope oscillator, Phys. Scr. **97**, 085211 (2022).

[34] S. Paul and R. D. Shankar, Vibrational resonance in a driven two-level quantum system, linear and nonlinear response, Philos. Trans. Roy. Soc. A **379**, 20200231 (2021).

[35] B. I. Usama, S. Morfu, and P. Marquie, Vibrational resonance and ghost-vibrational resonance occurrence in Chua's circuit models with specific nonlinearities, Chaos Solitons Fract. **153**, 111515 (2021).

[36] J. M. Aguessivognon, C. H. Miwadinou, and A. V. Monwanou, Effect of biharmonic excitation on complex dynamics of a two-degree-of-freedom heavy symmetric gyroscope, Phys. Scr. **98**, 095230 (2023).

[37] C. Adéyémi, Y. J. F. Kpomahou, J. K. Agbélélé, A. J. Adéchinan, and A. E. Yamadjako, Effects of periodic parametric damping and amplitude-modulated signal on vibrational resonance and torus-doubling bifurcations occurrence in an asymmetric mixed Rayleigh-Liénard oscillator, Phys. Scr. **98**, 105204 (2023).

[38] S. Bennett, C. Snowden, and S. Iezekiel, Nonlinear dynamics in directly modulated multiple-quantum-well laser diodes, IEEE J. Quantum Electron. **33**, 2076 (1997).

[39] C. Mayol, R. Toral, C. Mirasso, S. Turovets, and L. Pesquera, Theory of main resonances in directly modulated diode lasers, IEEE J. Quantum Electron. **38**, 260 (2002).

[40] K. C. Yee, M. Y. Chua, and K. Voon, Sidelobes reduction using simple two and tri-stages non linear frequency modulation (NLFM), Prog. Electromagn. Res. **98**, 33 (2009).

[41] M. A. Nashrin, S. M. A. Kader, M. V. S. Meenakshi, V. Chinnathambi, and S. Rajasekar, Analysis of vibrational resonance in a parametric quintic oscillator with double-well potentials, Dynamic Syst. & Appl. **32**, 294 (2023).

[42] O. T. Kolebaje, U. E. Vincent, B. E. Benyeogor, and P. V. E. McClintock, Effect of a modulated acoustic field on the dynamics of a vibrating charged bubble, Ultrasonics **135**, 1 (2023).

[43] A. Pikovsky and F. Bagnoli, Dynamics of oscillator populations with disorder in the coupling phase shifts, New J. Phys. **26**, 023054 (2024).

[44] M. Chatzittofi, J. Agudo-Canalejo, and R. Golestanian, Nonlinear response theory of molecular machines, Europhys. Lett. **147**, 21002 (2024).

[45] E. Kurt and M. Canturk, Chaotic dynamics of resistively coupled DC-driven distinct Josephson junctions and the effects of circuit parameters, Physica D **238**, 2229 (2009).

[46] P. Durandetto and A. Sosso, Using a Josephson junction as an effective on-chip temperature sensor, Supercond. Sci. Technol. **34**, 045008 (2021).

[47] I. K. Ngongiah, B. Ramakrishnan, Z. T. Njitacke, G. F. Kuiate, and S. T. Kingni, Resistive–capacitive shunted Josephson junction with unharmonic current-phase relation: Analysis and microcontroller implementation, Physica A **603**, 127757 (2022).

[48] P. O. Adesina, U. E. Vincent, T. O. Roy-Layinde, O. T. Kolebaje, and P. V. E. McClintock, Crisis-induced vibrational resonance in a phase-modulated periodic structure, Phys. Rev. E **110**, 034215 (2024).

[49] J. Lynch and R. York, A mode locked array of coupled phase locked loops, IEEE Microw. Guided Wave Lett. **5**, 213 (1995).

[50] A. Slavin, Spin-torque oscillators get in phase, Nat. Nanotechnol. **4**, 479 (2009).

[51] H.-K. Chen, Chaos and chaos synchronization of a symmetric gyro with linear-plus-cubic damping, J. Sound Vib. **255**, 719 (2002).

[52] B. A. Idowu, U. E. Vincent, and A. N. Njah, Synchronization of chaos in non-identical parametrically excited systems, Chaos, Sol. Fract. **39**, 2322 (2009).

[53] B. S. Dandogbessi and A. Kenfack, Absolute negative mobility induced by potential phase modulation, Phys. Rev. E **92**, 062903 (2015).

[54] F. Sattari and S. Mirershadi, Transport properties in a monolayer MoS_2 with time-periodic potential, Indian J. Phys. **97**, 2363 (2023).

[55] F. Sattari and S. Mirershadi, Spin-valley-dependent transport in a monolayer MoS_2 under strain and time-oscillating potential, Physica B **662**, 414975 (2023).

[56] B. Li, B. Bai, T. Aulin, and Q. Li, Advanced continuous phase modulation for high mobility communications, Chin. Sci. Bull. **59**, 4999 (2014).

[57] S. Bovetti and T. Fellin, Optical dissection of brain circuits with patterned illumination through the phase modulation of light, J. Neurosci. Methods **241**, 66 (2015).

[58] R. A. Bartels, T. C. Weinacht, N. Wagner, M. Baertschy, C. H. Greene, M. M. Murnane, and H. C. Kapteyn, Phase modulation of ultrashort light pulses using molecular rotational wave packets, Phys. Rev. Lett. **88**, 013903 (2001).

[59] D. F. Gordon, B. Hafizi, R. F. Hubbard, J. R. Peñano, P. Sprangle, and A. Ting, Asymmetric self-phase modulation and compression of short laser pulses in plasma channels, Phys. Rev. Lett. **90**, 215001 (2003).

[60] D. F. Gordon, B. Hafizi, R. F. Hubbard, J. R. Penano, P. Sprangle, and A. Ting, Asymmetric self-phase modulation and compression of short laser pulses in plasma channels, Phys. Rev. Lett. **90**, 215001 (2003).

[61] A. Feist, K. E. Echternkamp, J. Schauss, S. V. Yalunin, S. Schäfer, and C. Ropers, Quantum coherent optical phase modulation in an ultrafast transmission electron microscope, Nature **521**, 200 (2015).

[62] D. H. White, S. K. Ruddell, and M. D. Hoogerland, Experimental realization of a quantum ratchet through phase modulation, Phys. Rev. A **88**, 063603 (2013).

[63] D. Anastasio and S. Marchesiello, Nonlinear frequency response curves estimation and stability analysis of randomly excited systems in the subspace framework, Nonlinear Dyn. **111**, 8115 (2023).

[64] R. Jothimurugan, K. Thamilmaran, S. Rajasekar, and M. A. F. Sanjuán, Multiple resonance and anti-resonance in coupled Duffing oscillators, Nonlinear Dyn. **83**, 1803 (2016).

[65] R. Samikkannu, M. Ramasamy, S. Kumarasamy, and K. Rajagopal, Studies on ghost-vibrational resonance in a periodically driven anharmonic oscillator, Eur. Phys. J. B. **96**, 56 (2023).

[66] Y. Antonenas, G. Anastassiou, and Y. Kominis, Analytical calculation of the kinetic q factor and resonant response of toroidally confined plasmas, Phys. Plasmas **31** (2024).

[67] P. Ashokkumar, R. Kabilan, M. Sathish Aravindh, A. Venkatesan, and M. Lakshmanan, Harnessing vibrational resonance to identify and enhance input signals, Chaos **34** (2024).

[68] A. Abbas, J. De Vicente, and E. Valero, Aerodynamic technologies to improve aircraft performance, Aerosp. Sci. Technol. **28**, 100 (2013).

[69] T. Wang, J. Dupont, and J. Tang, On integration of vibration suppression and energy harvesting through piezoelectric shunting with negative capacitance, IEEE Trans. Magn. Mechatronics **28**, 2621 (2023).

[70] Z. Zhang, H. Ding, Y.-W. Zhang, and L.-Q. Chen, Vibration suppression of an elastic beam with boundary inerter-enhanced nonlinear energy sinks, Acta Mech. Sin. **37**, 387 (2021).

[71] Z. Zhang, Z.-T. Gao, B. Fang, and Y.-W. Zhang, Vibration suppression of a geometrically nonlinear beam with boundary inertial nonlinear energy sinks, Nonlinear Dyn. **109**, 1259 (2022).

[72] E. Livne, Aircraft active flutter suppression: State of the art and technology maturation needs, J. Aircr. **55**, 410 (2018).

[73] L. Wang, Y. Pan, K. Li, L. He, Q. Wang, and W. Wang, Modeling and reliability analysis of mems gyroscope rotor parameters under vibrational stress, Micromachines **15**, 648 (2024).

[74] J. Guo, C. J. Damaren, and Y. Geng, Space structure vibration suppression using control moment gyroscope null motion, J. Guid. Control Dyn. **42**, 2272 (2019).

[75] M. Ge, K. Yu, Y. Wu, D. Wang, G. Wang, and C. Yu, Review of micro-vibration modeling, suppression, and measurement for spacecraft with high-precision, in *Signal and Information Processing, Networking and Computers*,

edited by Y. Wang, Y. Liu, J. Zou, and M. Huo (Springer Nature Singapore, Singapore, 2023) pp. 787–796.

[76] A. Staino and B. Basu, Emerging trends in vibration control of wind turbines: a focus on a dual control strategy, Philos. Transact. A Math. Phys. Eng. Sci. **373**, 20140069 (2015).

[77] N. El-Sheimy and A. Youssef, Inertial sensors technologies for navigation applications: State of the art and future trends, Satell. Navig. **1**, 2 (2020).

[78] W. A. Gill, I. Howard, I. Mazhar, and K. McKee, A review of mems vibrating gyroscopes and their reliability issues in harsh environments, Sensors **22**, 7405 (2022).

[79] K. Larkin, M. Ghommem, M. Serrano, and A. Abdelkefi, A review on vibrating beam-based micro/nano-gyroscopes, Microsyst. Technol. **27**, 4157 (2021).